

RESEARCH ARTICLE

Realistic efficiency potential of next-generation industrial Czochralski-grown silicon solar cells after deactivation of the boron–oxygen-related defect center

Dominic C. Walter^{1*}, Bianca Lim¹ and Jan Schmidt^{1,2}¹ Institute for Solar Energy Research Hamelin (ISFH), Am Ohrberg 1, D-31860 Emmerthal, Germany² Department of Solar Energy, Institute of Solid-State Physics, Leibniz Universität Hannover, Appelstraße 2, 30607 Hannover, Germany

ABSTRACT

We measure carrier lifetimes of different Czochralski-grown silicon (Cz-Si) materials of various boron and oxygen concentrations and determine the maximum achievable lifetime after an optimized thermal treatment. We obtain very high and stable bulk lifetimes of several milliseconds, virtually eliminating the boron–oxygen (BO) defect complex, which previously limited the carrier lifetime in boron-doped Cz-Si materials after prolonged illumination. Based on these experimental results, we introduce a new parameterization of the bulk lifetime of B-doped Cz-Si after permanent deactivation of the BO center. Notably, we measure lifetimes up to 4 ms on 2- Ω cm Cz-Si wafers at an injection level of 1/10 of the doping concentration. Importantly, these high lifetime values can be reached within 10 and 20 s of BO deactivation treatment. A detailed analysis of the injection-dependent lifetimes reveals that the lifetimes after permanent deactivation of the BO center can be well described by a single-level recombination center characterized by an electron-to-hole capture cross-section ratio of 12 and located in the middle of the silicon band gap. We implement the novel parameterization into a two-dimensional device simulation of a passivated emitter and rear solar cell using technologically realistic cell parameters. The simulation reveals that based on current state-of-the-art solar cell production technology, efficiencies reaching 22.1% are realistically achievable in the near future after complete deactivation of the BO center. Copyright © 2016 John Wiley & Sons, Ltd.

KEYWORDS

silicon; lifetime; permanent recovery; boron–oxygen defect; Czochralski–silicon; PERC

*Correspondence

Dominic C. Walter, Institute for Solar Energy Research Hamelin (ISFH), Am Ohrberg 1, D-31860 Emmerthal, Germany.

E-mail: d.walter@isfh.de

Received 23 July 2015; Revised 9 November 2015; Accepted 18 November 2015

1. INTRODUCTION

Screen-printed solar cells with a full-area Al- p^+ back surface field (Al-BSF cells) made on boron-doped Czochralski-grown silicon (Cz-Si) or multicrystalline silicon wafers are the industrial standard in today's silicon solar cell production [1]. However, as the performance of this cell type is limited by the relatively high recombination losses at the fully metalized rear side of the cell, in the next couple of years, it is expected that Al-BSF cells will be gradually replaced in production by the 'passivated emitter and rear cell' (PERC) design [2,3]. In this advanced cell design, the rear side of the solar cell is passivated by a dielectric layer (typically a stack of Al₂O₃ and SiN_x [4] or a stack of SiO₂ and SiN_x [5,6]) with only local metal-contacted

areas at the rear. Thereby, the overall surface recombination losses at the rear side are drastically reduced, and hence, the conversion efficiency potential is significantly increased. However, the reduction in the recombination at the rear surface increases the sensitivity of the solar cell to other recombination channels, such as the bulk recombination [7]. Hence, the actual increase in cell efficiency between the two cell designs critically depends on the bulk material quality.

Recently, we examined the impact of bulk recombination losses on the performance of Al-BSF versus PERC solar cells for a variety of impurities being present in the bulk material [7]. It was shown that apart from metal impurities, the boron–oxygen (BO)-related defect center [8–10] is the most harmful defect in boron-doped Czochralski-grown

silicon. The BO recombination center is fully activated during prolonged illumination [11]; however, it can be permanently deactivated by illumination at elevated temperatures [12]. The implementation of a lifetime parameterization based on lifetime measurements after permanent deactivation of the BO center into a two-dimensional device simulation revealed an efficiency potential of PERC solar cells of 20.7 % [7]. More recently, we further optimized the process of permanent deactivation of the BO recombination center [13]. By applying the optimized treatment, we were able to realize carrier lifetimes significantly exceeding the lifetimes reported in our previous publication [7]. In the present contribution, we introduce a new parameterization of the carrier lifetime as a function of doping concentration and injection level after application of the optimized permanent deactivation procedure. We apply the revised lifetime parameterization to two-dimensional device simulations, representing an industrially producible state-of-the-art PERC structure, which we consider the as next-generation industrial solar cell, and show that efficiencies greater than 22% are realistically achievable.

2. MILLISECOND LIFETIMES IN BORON-DOPED CZ-SI WAFERS

The carrier lifetime of boron-doped Cz-Si is known to significantly degrade upon illumination because of the activation of a BO defect complex and eventually limits the efficiency of solar cells made on this material [8,10,14]. A permanent recovery of the lifetime, that is, a permanent deactivation of the BO defect, is possible by illumination at elevated temperature [12] or, in general, by the injection of minority carriers at elevated temperature. Currently, two different hypotheses exist on the underlying physical mechanism of the deactivation process. First, it is assumed that the fast-firing step with a hydrogen-rich dielectric layer on the surfaces of the sample causes the diffusion of hydrogen from the surfaces into the silicon bulk, which then passivates the defect center through a direct hydrogenation [15,16]. Second, it is assumed that the fast cooling during the fast-firing process step produces a favorable configuration of boron–nano-precipitates [13,17]. During the recovery process, free interstitial boron atoms dissociate from the defect complex, leave a non-recombination-active complex, and sink into these precipitates without the involvement of hydrogen.

Independent of the actual physical mechanism, the lifetime, which can be reached after the process of permanent deactivation depends on the exact thermal history of the sample, especially on the temperature treatments immediately before the actual recovery process, is applied [18]. As we have shown recently, by applying a fast-firing step in an industrial belt-firing furnace directly before the permanent deactivation process, the lifetime achieved after completed permanent deactivation shows a pronounced dependence on the belt speed of the furnace [13].

Importantly, we observed that the highest lifetimes after complete permanent deactivation are obtained for the fastest belt speed applied [18]. As the observed lifetimes even with the fastest belt speed are still considerably below the intrinsic lifetime limit, one might speculate about lifetime-limiting background defects. Possible candidates would be, for example, oxygen clusters or boron precipitates. However, more detailed studies would be required to identify the true nature of these defects following the approach outlined in Reference [19].

In order to examine the achievable lifetimes after permanent recovery as a function of the boron doping concentration, we have processed five different commercially available boron-doped Cz-Si materials with resistivities between 0.5 and 5 Ωcm into lifetime samples. The measured interstitial oxygen concentration $[O_i]$, determined via FTIR measurements (IOC 88), varies between 5×10^{17} and $10 \times 10^{17} \text{ cm}^{-3}$, representing a typical range for Cz-Si. Sample processing included the removal of the surface damage using an aqueous solution of KOH, which was followed by a standard RCA cleaning sequence. Afterwards, all samples underwent a phosphorus diffusion (850 °C, 1 h) resulting in a sheet resistance of the diffused n^+ -regions of $\sim 100 \Omega/\square$. After the removal of the phosphosilicate glass using HF, the n^+ -diffused regions were removed using KOH. After RCA cleaning, the wafer surfaces were passivated by a stack of aluminum oxide (Al_2O_3) and silicon nitride (SiN_x) [4]. Ten nanometer of Al_2O_3 , deposited via plasma-assisted atomic layer deposition using an Oxford Instruments FlexALTM reactor, were deposited underneath a 70-nm-thick SiN_x layer (refractive index $n = 2.05$), which was deposited by plasma-enhanced chemical vapor deposition using a Roth & Rau SiNA system. After deposition of the dielectric passivation layers, the samples underwent a fast-firing step in a commercially available belt firing furnace (Centrotherm). For the determination of the ultimate lifetime limit, the firing parameters were set at a peak temperature of 850 °C and a maximum belt speed of 7.2 m/min. Please note that the actual peak temperature of the wafer, which we measured using a temperature probe attached to lifetime samples of the same material processed in parallel, was only in the range of $(775 \pm 20)^\circ\text{C}$.

After sample processing, we performed the permanent BO deactivation (also known as ‘recovery’ process) by illuminating the samples at a light intensity of 100 mW/cm^2 using a halogen lamp. The samples were placed on a hotplate at various temperatures between 130 and 230 °C during illumination. As we have shown in a recent contribution [18], in contrast to the belt speed, the temperature of the permanent recovery process does not affect the lifetime reached after the recovery process in the applied temperature interval.

The carrier lifetimes during the recovery process are continuously monitored by removing the samples after defined time intervals from the hotplate and measuring the lifetime at room temperature by the photoconductance decay method using a Sinton lifetime tester (WCT-120) [20]

until the lifetimes saturate. The lifetime values reported in this paper are, apart from the injection-dependent lifetimes, extracted at a fixed injection level of $\Delta n/p_0 = 0.1$, with Δn being the excess carrier density and p_0 being the hole concentration in darkness, which equals in boron-only doped material the doping concentration N_{dop} .

The maximum effective lifetimes reached after completing the deactivation process, that is, after full deactivation of the BO defect, are shown in Figure 1 (blue diamond) as a function of the doping concentration. On lifetime samples processed in parallel on 1.3 Ωcm boron-doped float-zone silicon as well as on 0.8 Ωcm gallium-doped Cz-Si, we extracted surface recombination velocities below 1 cm/s. Therefore, we assume that the measured effective lifetimes equal the bulk lifetimes of the investigated boron-doped Cz-Si materials. Please note that this may underestimate the actual bulk lifetime if the assumption does not hold. In that case, the lifetimes measured here have to be considered as a lower limit to the bulk lifetime. For comparison, the intrinsic lifetime limit, as recently published by Richter *et al.* (solid black line) [21], as well as the lifetime limit after permanent deactivation, as previously published by Schmidt *et al.* (dashed light red line) [7] are also shown in Figure 1. Please note that if no recovery process is applied, the lifetime after complete degradation is represented by the orange dashed-dotted line according to the parameterization by

Bothe *et al.* [9] at a typical interstitial oxygen concentration of $[O_i] = 7.5 \times 10^{17} \text{ cm}^{-3}$. In this case, an enhancement factor of 2 was multiplied to the lifetime parameterization of Reference 9, accounting for the phosphorus diffusion the samples underwent during processing. However, the actual lifetimes after complete degradation depend also critically on the fast-firing process, which leads to an additional lifetime improvement [18]. Therefore, the low lifetimes shown as dash-dotted line in Figure 1 can be considered as worst-case scenario.

The lifetimes measured in this study significantly exceed the previously published lifetimes on boron-doped Cz-Si. Note that for the technologically important materials with resistivities around 1 Ωcm , the lifetimes measured in this contribution are a factor of 20 larger than predicted by the previous lifetime limit of Reference 7 represented by the dashed red line in Figure 1. The main difference of the samples presented here compared with our previous parameterization in Reference 7 is the presence of the optimized fast-firing step, which is required to reach maximum lifetimes after permanent recovery [18].

The dependence of the lifetime τ after permanent deactivation of the BO center on the hole concentration p_0 , at an injection density of $\Delta n = 0.1 \times p_0$, can be described by the following parameterization (solid blue line in Figure 1):

$$\begin{aligned} \tau(\Delta n = 0.1 \times p_0) &= \left(\frac{1}{\tau_1} + \frac{1}{\tau_2} \right)^{-1} \\ &= \left(\frac{1}{5500 \text{ } \mu\text{s}} + \frac{p_0^2}{5 \times 10^{35} [\text{cm}^{-6} \text{ } \mu\text{s}]} \right)^{-1}. \end{aligned} \quad (1)$$

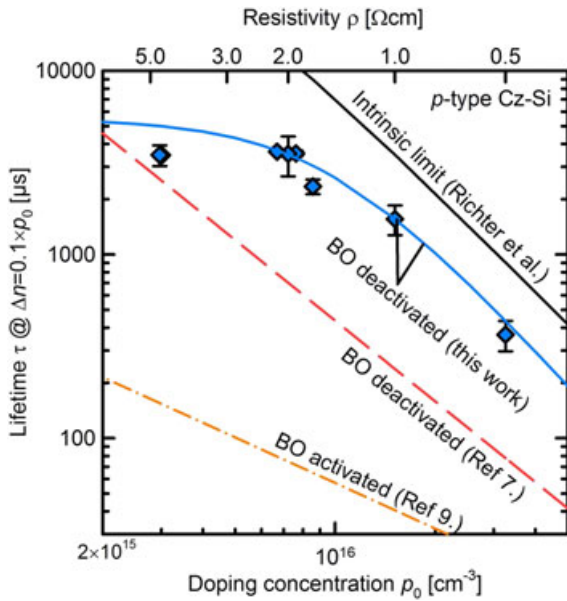


Figure 1. Measured lifetimes τ at a fixed injection density $\Delta n = 0.1 \times p_0$ after permanent deactivation (blue diamond) versus doping concentration p_0 . For comparison, the lifetime parameterization after complete degradation according to Bothe *et al.* (orange dashed-dotted line), the lifetime parameterization after permanent deactivation according to Schmidt *et al.* (red dashed line), and the intrinsic lifetime limit according to Richter *et al.* (black solid line) are also displayed. The blue solid line gives the dependence of the lifetime after permanent deactivation according to our newly proposed parameterization shown in Eq. (1).

In addition to the lifetime values at the fixed injection level of $\Delta n/p_0 = 0.1$, our data also allow to extract the complete injection dependence of the lifetimes after permanent recovery. The full injection dependence of the lifetimes can be quite well described by a single Shockley–Read–Hall (SRH) [22] recombination center in addition to the intrinsic lifetime limit (including Auger and radiative recombination) according to Richter *et al.* [21]. The SRH center is located in the middle of the silicon band gap and the electron-to-hole capture cross-section ratio is $\frac{\sigma_n}{\sigma_p} = 12$. Please note that the lifetime analysis performed here is not intended to comprehensively describe the defect physics involved in the deactivation process but to systematically describe the measured lifetime curves in the low-injection regime relevant to solar cell operation.

In general, the SRH lifetime of a single level center is described by the expression

$$\tau_{\text{SRH}} = \frac{\tau_{p0} \times (n_0 + n_1 + \Delta n) + \tau_{n0} \times (p_0 + p_1 + \Delta n)}{(n_0 + p_0 + \Delta n)}, \quad (2)$$

where n_1 and p_1 are the SRH densities, which depend on the energy level of the defect center in the silicon band gap, and τ_{n0} and τ_{p0} are the capture time constants of electrons and holes, respectively. These capture time constants

are inversely proportional to the respective capture cross section, thus $\frac{\tau_{n0}}{\tau_{p0}} = \frac{\sigma_p}{\sigma_n} = \frac{1}{12}$ in our case. Restricting the analysis to excess carrier concentrations of $\Delta n \gg 10^{10} \text{ cm}^{-3}$ and exploiting the fact that in our case the defect energy level is assumed to be in the middle of the band gap ($p_1 \ll p_0 + \Delta n$ and $n_1 \ll \Delta n$), the SRH lifetime for p -type silicon ($p_0 \gg n_0$) can be written as [23]

$$\begin{aligned} \tau_{\text{SRH}}(p_0, \Delta n) &= \frac{\tau_{p0} \times \Delta n + \tau_{n0} \times (p_0 + \Delta n)}{(p_0 + \Delta n)} \\ &= \tau_{p0} \times \left(\frac{1}{\eta^{-1} + 1} + \frac{\tau_{n0}}{\tau_{p0}} \right) \\ &= \tau_{p0} \times \left(\frac{1}{\eta^{-1} + 1} + \frac{1}{12} \right), \end{aligned} \quad (3)$$

with $\eta \equiv \frac{\Delta n}{p_0}$ being the injection level. At a fixed injection level of $\eta = 0.1$, we obtain

$$\tau_{\text{SRH}}(\eta = 0.1) = \frac{23}{132} \times \tau_{p0}. \quad (4)$$

Using this equation, as well as the expression for the measured lifetime $\tau^{-1}(\eta) = \tau_{\text{int}}^{-1}(\eta) + \tau_{\text{SRH}}^{-1}(\eta)$ with τ_{int} being the intrinsic lifetime, we obtain for the hole capture time constant τ_{p0} determined at a constant injection level of $\eta = 0.1$

$$\begin{aligned} \tau_{p0} &= \frac{132 \times \tau_{\text{SRH}}(\eta = 0.1)}{23} \\ &= \frac{132}{23} \left(\frac{1}{\tau(\eta = 0.1)} - \frac{1}{\tau_{\text{int}}(\eta = 0.1)} \right)^{-1}. \end{aligned} \quad (5)$$

Hence, we obtain the complete injection-dependent lifetime by inserting this Eq. (5) into Eq. (3):

$$\begin{aligned} \tau_{\text{SRH}}(p_0, \eta) &= \left(\frac{1}{\tau(\eta = 0.1)} - \frac{1}{\tau_{\text{int}}(\eta = 0.1)} \right)^{-1} \\ &\quad \times \left(\frac{132}{23 \times (\eta^{-1} + 1)} + \frac{11}{23} \right). \end{aligned} \quad (6)$$

For the intrinsic lifetime τ_{int} , we use the parameterization by Richter *et al.*, which is given for material with $p_0 < 6 \times 10^{16} \text{ cm}^{-3}$ (i.e., for resistivities exceeding $0.3 \text{ } \Omega\text{cm}$) by [24]:

$$\tau_{\text{int}} = \frac{\Delta n}{np(8.7 \times 10^{-29} n_0^{0.91} + 6.0 \times 10^{-30} p_0^{0.94} + 3.0 \times 10^{-29} \Delta n^{0.92} + B_{\text{low}})}, \quad (7)$$

with $B_{\text{low}} = 4.73 \times 10^{-15}$. Please note that the electron and hole densities must be given per cubic centimeter in order to obtain the intrinsic lifetime in the unit of seconds.

All the measured injection-dependent lifetimes after permanent recovery within this study are well described by this parameterization. An example is given in Figure 2, which shows the injection-dependent lifetimes of three

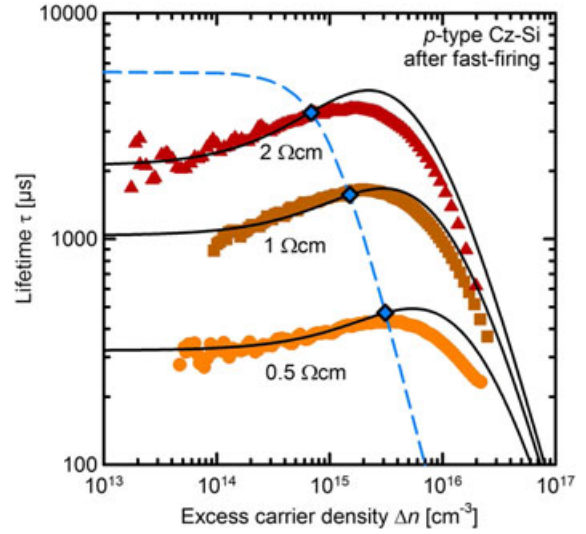


Figure 2. Measured injection-dependent carrier lifetime $\tau(\Delta n)$ of three differently doped materials (colored symbols) studied in this investigation. The blue dashed line is the dependence described by our novel parameterization (Eq. (11)). The black solid lines are calculated using the SRH equation and assuming a single-level recombination center at midgap with a capture cross-section ratio σ_n/σ_p of 12, including the intrinsic lifetime limit.

differently doped samples with resistivities ranging from 0.5 to $2.0 \text{ } \Omega\text{cm}$. The calculated lifetimes using Eq. (6) (black solid lines) are in good agreement with the measured injection-dependent lifetimes of the three exemplary materials.

3. PERMANENT DEACTIVATION OF THE BO RECOMBINATION CENTER

For industrial applications, it is important to reach the high lifetimes mentioned earlier in as small as possible time frame. Therefore, an optimized thermal pre-treatment is required [25]. In particular, a fast cooling ramp at 600°C is very important to minimize the process time of the recovery process [13].

The rate constant R_{de} of the deactivation process can be used as a measure for the period needed for the recovery of the lifetime. Thereby, R_{de} is defined by the single exponential dependence $A \times \exp(-R_{\text{de}} \times t) + B$, which is used to fit the change of the effective defect concentration $N_t^* \equiv \frac{1}{\tau(t)} - \frac{1}{\tau_0}$, with $\tau(t)$ being the measured lifetime at the time t during the recovery process and τ_0 the lifetime measured after annealing in darkness at 200°C for 10 min (temporary deactivation of the BO center). All lifetime measurements are performed at room temperature. A variation of the belt speed during the firing process at a constant set peak temperature of 850°C facilitates different cooling rates $-\frac{dT}{dt}$ at 600°C . Each individual cooling rate was measured with a temperature probe attached to a sample processed in parallel

to the sample under investigation. Figure 3 shows the recovery rate constants R_{de} versus various measured cooling rates at 600 °C after firing. We observe an increasing rate constant R_{de} with an increasing cooling rate $-\frac{d\vartheta}{dt}$ for all investigated materials, which emphasizes the general validity of the findings in Reference 13. Interestingly, the recovery rate constants determined on 1.0 Ωcm material are lower than the rate constants measured for the materials of higher resistivities, but no unambiguous dependence on the doping concentration p_0 can be extracted from our results. The gray dashed lines are guides to the eye of the expected linear behavior [13]. The different slopes of the dashed lines may indicate that apart from the cooling rate at 600 °C, another parameter exists which additionally influences the recovery rate constant, however, to a much weaker extent than the cooling rate. One may speculate that a dependence on the resistivity up to resistivities in the range of 1.7 Ωcm exists, especially when considering our results on 0.5 Ωcm material, which show for the highest cooling rate at a much smaller recovery rate constant. Therefore, further investigations are needed to clarify this possible correlation with the doping concentration.

From previous studies, it is known that increasing the recovery temperature [18,26], as well as increasing the illumination intensity [27] during the recovery process, further increases the recovery rate constant, that is, shortens the recovery period. Additionally, it was shown by Wilking *et al.* [16] that an additional annealing step in darkness after the fast firing at intermediate temperatures between 200 and 400 °C leads to a further reduction of

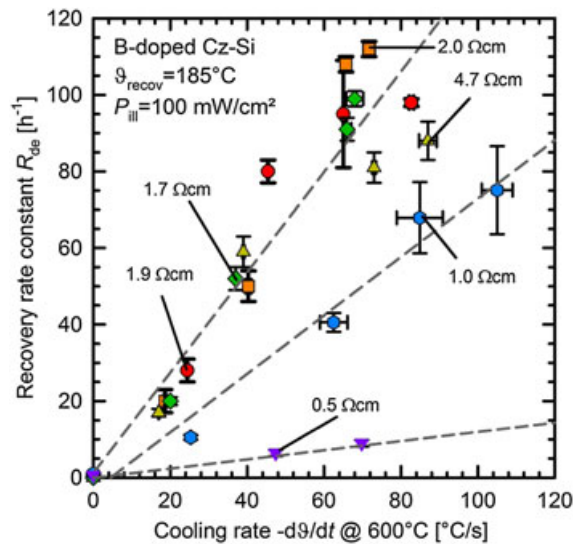


Figure 3. Recovery rate constant R_{de} versus cooling rate $-\frac{d\vartheta}{dt}$ at 600 °C during the firing process for various silicon materials relevant for solar cell production. The base resistivity varies between 0.5 and 4.7 Ωcm . For all materials, R_{de} increases with increasing cooling rate. The gray dashed lines are guides to the eye.

the recovery period. We included all these findings into our experiments by annealing the samples after firing at 250 °C for 10 min in darkness and by performing the recovery process at an elevated temperature of 230 °C at 245 mW/cm^2 light intensity. Figure 4 shows the recovery of the lifetime during the annealing under illumination for three samples. The filled triangles correspond to a sample treated as mentioned before, while the sample corresponding to the open triangles was annealed at 200 °C and recovered at 185 °C and 100 mW/cm^2 (1 sun) light intensity. The improved conditions clearly further accelerate the recovery process. On another sample with a higher resistivity of 4.7 Ωcm (circles in Figure 4), which was also treated by the improved conditions, we do not observe the typical degradation of the lifetime followed by its recovery. The lifetime remains stable at values above 2.5 ms. As the first data point was measured after 5 s of deactivation treatment, we conclude that the deactivation process was already completed within the first 5 s.

4. TWO-DIMENSIONAL DEVICE SIMULATIONS

In order to estimate the impact of our new lifetime parameterization on the performance of next-generation industrial silicon solar cells, we perform two-dimensional device simulations using the Quokka simulation tool [28], which is based on the conductive boundary model

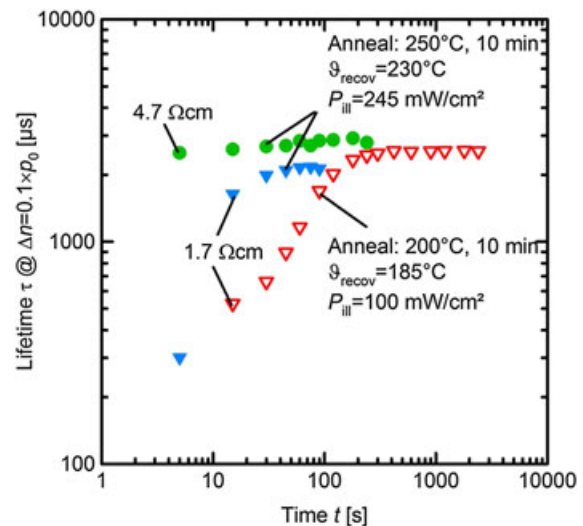


Figure 4. Measured lifetimes τ at a fixed injection density $\Delta n = 0.1 \times p_0$ as a function of illumination time t during the recovery process. Open triangles correspond to a sample after annealing at 200 °C in darkness for 10 min and subsequently recovered at 185 °C and 100 mW/cm^2 light intensity. Filled triangles and circles correspond to two other samples after 250 °C annealing in darkness and recovered at 230 °C and 245 mW/cm^2 light intensity.

introduced by Brendel [29]. We simulate PERC solar cells with a total thickness of 180 μm and a homogeneous front-side n^+ -diffusion with a sheet resistance of $80 \Omega/\square$. A schematic of the simulated cell structure is shown in Figure 5. Furthermore, we assume a random pyramid front texture, which is coated by a 70-nm-thick SiN_x layer (refractive index $n=2.03$). The line width of the metal finger on the front side is chosen to 55 μm , which has already been shown to be achievable using industrial printing technology [3]. Additionally, we assume a 5-busbar design with an overall front side shading of 4%, which has recently been demonstrated for such a design [30]. At the rear side, we assume a good rear surface passivation using, for example, a stack of Al_2O_3 and SiN_x . The rear side is then assumed to be full-area screen-printed with an aluminum paste. Line openings in the dielectric layer stack are assumed to be made by, for example, laser ablation with a contact opening width of 100 μm [3]. A subsequent fast-firing step leads to the formation of a local back surface field. The general input parameters such as the spacing and the saturation current densities J_0 are summarized in Table I. We have chosen typical values for the J_0 values, which have been shown to be achievable in today's state-of-the-art screen-printed solar cells [31].

Figure 6(a) shows the simulated conversion efficiencies η for a constant pitch p of the metal contact lines of 2 mm on the front and back as a function of the doping concentration p_0 , to compare the results of this contribution with our previous results [7]. In Figure 6(b), an optimization of the front and rear side pitch in terms of the conversion efficiency has been performed for each simulated data point.

For the constant pitch of 2 mm at the front and rear [Figure 6(a)], the Quokka simulation reveals that the optimum resistivity is shifted towards lower resistivities compared with our previously published results [7]. For the optimal resistivity of $0.75 \Omega\text{cm}$, a maximum efficiency of 21.9% is achieved. Compared with that, the optimal resistivity according to Reference 7 was in the range between 1 and $2 \Omega\text{cm}$. The decrease of the efficiency towards both sides of the maximum efficiency is dominated by two different mechanisms. Towards higher

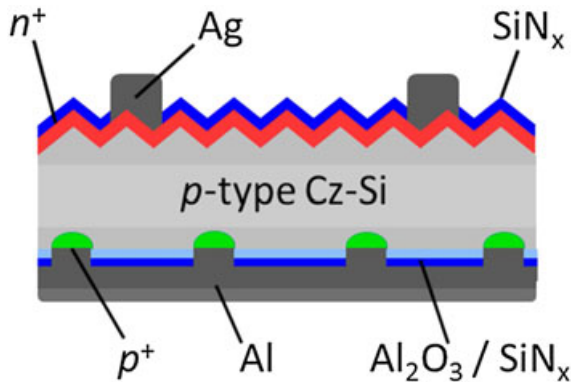


Figure 5. Schematic of the simulated passivated emitter and rear solar cell.

Table I. Input parameters for the 2D Quokka simulations.

Parameters	
Cell thickness w	180 μm
Series resistance $R_{S,\text{Finger}}$ (only finger contribution)	100 $\text{m}\Omega\text{cm}^2$
Front side	
Front contact width p_{front}	55 μm
n^+ sheet resistance ρ_{n^+}	80 Ω/\square
Junction depth x_j	0.62 μm
Saturation current density of contacted area J_{0,cont,n^+}	500 fA/cm^2
Saturation current density of passivated area J_{0,pass,n^+}	125 fA/cm^2
Contact resistance R_c	2 $\text{m}\Omega\text{cm}^2$
Rear side	
Rear contact width p_{rear}	100 μm
Sheet resistance beneath contact ρ_{p^+}	35 Ω/\square
Junction depth x_{p^+}	4 μm
Contact resistance R_{c,p^+}	8 $\text{m}\Omega\text{cm}^2$
Saturation current density of contacted area J_{0,met,p^+}	650 fA/cm^2
Saturation current density of passivated area $J_{0,\text{pass, rear}}$	25 fA/cm^2

The saturation current densities are extracted from measurements on fabricated solar cells [30,31].

doping concentrations, that is, lower resistivities, the efficiency decreases because of a reduction of the bulk lifetime. Towards lower doping concentrations, that is, higher resistivities, the efficiency decreases because of lateral resistive losses of the majority carriers in the silicon bulk.

The latter limitation can be overcome by a reduction of the contact line distance on the rear side. This can be seen in Figure 6(b), where the contact distances on the front and rear side are varied independently to obtain the highest efficiency for each base resistivity. For the efficiency curves corresponding to the lifetimes after complete degradation (orange squares) and to the lifetimes after permanent recovery as presented in Reference 7 (red triangles), the maximum efficiency is shifted towards higher resistivities, greater than $4 \Omega\text{cm}$. For our novel lifetime parameterization (blue circles), the pitch optimization does not shift the maximum efficiency significantly towards higher resistivities, but widens the range of resistivities with maximum efficiencies now reaching 22.1%, for a finger distance of 1.8 mm at the front and a line pitch of 1.2 mm at the cell rear. The simulation unambiguously reveals that if the contact line distances at the front and back side are optimized, efficiencies of 22% can be reached for an extremely broad range of base resistivities between 0.5 and $3 \Omega\text{cm}$.

The fact that the blue curve decreases towards lower resistivities is, again, an effect of the bulk lifetime. The parameterization of the lifetime after permanent deactivation according to Reference 7 predicts a continuously increasing lifetime towards lower doping densities. Compared with that and according to Eq. (1), the lifetime parameterization presented in this study saturates at low doping densities at a lifetime of $\tau_1 = 5500 \mu\text{s}$. This leads to an

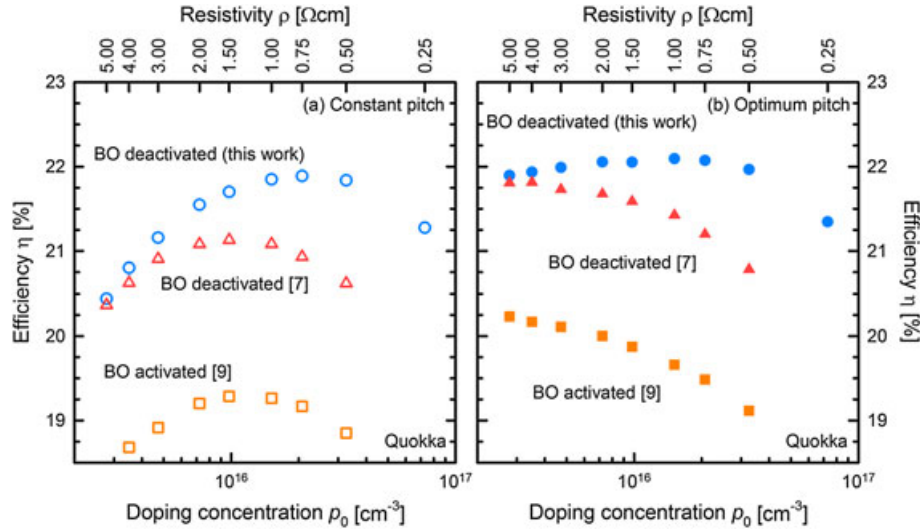


Figure 6. Simulated conversion efficiencies η versus base doping concentration p_0 (base resistivity ρ) using Quokka. (a) Efficiencies for the three different lifetime parameterizations shown in Figure 1 for a constant front and back pitch of 2 mm. (b) Efficiencies for the same lifetime parameterization with an optimum pitch at the front and back side.

intersection of the corresponding lifetime curves in Figure 1 (solid blue line and red dashed line) at doping densities p_0 between 10^{15} and $2 \times 10^{15} \text{ cm}^{-3}$. Therefore, in Figure 6(b), we obtain equal conversion efficiencies in this doping range for both parameterizations.

For the maximal simulated efficiency of 22.1% on $1.0 \Omega\text{cm}$ material, we performed a free energy loss analysis (FELA) [32]. The result of this analysis is shown in Figure 7 for the eight parameters with the highest contribution to the lost power density P_{lost} . From this analysis, we conclude that the lifetime according to our novel parameterization is not the limiting factor of the simulated conversion efficiency. The simulated efficiency is mainly limited by the saturation

current densities at the front side at the passivated n^+ -region J_{0, pass, n^+} and at the metalized p^+ -region on the rear side J_{0, met, p^+} , as well as by resistive losses in the n^+ -region on the front side ρ_{n^+} . Hence, the lifetimes based on our novel parameterization would allow conversion efficiencies exceeding 23% if these parameters were further optimized.

It is also interesting to take a closer look at the simulation results based on the completely degraded lifetimes shown in Figure 6(b). Obviously, conversion efficiencies above 20% can be obtained even in the fully degraded state if only lowly doped material with a specific resistivity above $2.0 \Omega\text{cm}$ is used. Note, however, that in this case, the line distance has to be adapted, for example, at a bulk resistivity of $2.0 \Omega\text{cm}$, a rear pitch of only 0.6 mm (front finger spacing of 1.8 mm) leads to an efficiency of 20.0%.

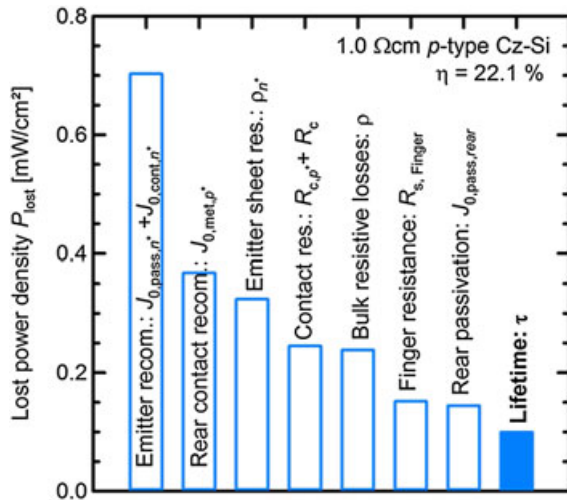


Figure 7. Lost power density P_{lost} according to the free energy loss analysis performed for the highest obtained conversion efficiency of 22.1%. The eight recombination parameters with the highest contribution to the lost power density are displayed.

5. CONCLUSIONS

In this paper, we have measured lifetimes on permanently recovered boron-doped Czochralski-grown silicon wafers, which significantly exceeded the maximum lifetimes reported previously. We obtain lifetimes of several milliseconds after an optimized thermal treatment, which consisted of a fast-firing process and an optimized permanent deactivation. Based on our measured lifetime data, we have developed a new parameterization of the lifetime as a function of the hole concentration. In addition, the injection dependence of the measured lifetimes after permanent recovery can be well modeled in the injection range relevant to solar cell applications using a single-level SRH center at midgap with an electron-to-hole capture cross-section ratio of $\frac{\sigma_n}{\sigma_p} = 12$.

In the second part of the paper, we have studied the industrial feasibility of a permanent recovery process. We

have shown that for all investigated Cz-Si materials, a faster cooling during the firing is beneficial for the recovery process. By optimizing the temperature treatment, we were able to achieve stable lifetimes larger than 2 ms after only 5 s of deactivation.

In the third part of this study, the impact of our new parameterization on the efficiency potential of next-generation industrial-type PERC solar cells was examined by performing 2D simulations using the Quokka simulation tool. The simulations revealed that very high efficiencies up to 22.1% are achievable using today's state-of-the-art processing techniques. Additionally, if the contact line spacing at the rear side of the PERC cells is optimized with respect to the base resistivity of the wafer, a very broad range of wafer resistivities, between 0.5 and 3 Ωcm , has a potential for conversion efficiencies of 22%. Finally, our simulations revealed that a further optimization of the cell design would allow to achieve even higher efficiencies in excess of 23% using boron-doped Cz-Si material.

ACKNOWLEDGEMENTS

This work was funded by the German State of Lower Saxony and the German Federal Ministry for Economics and Energy and by industry partners within the research project 'SolarLife' (contract no. 0325763C). The content is the responsibility of the authors.

REFERENCES

1. *International Technology Roadmap for Photovoltaic (ITRPV.net)*, 2015 Results, April 2015. Available at <http://www.itrpv.net/Reports/Downloads/2015>
2. Blakers AW, Wang A, Milne AM, Zhao J, Green MA. 22.8% efficient silicon solar cell. *Applied Physics Letters* 1989; **55**(13): 1363. DOI:10.1063/1.101596.
3. Dullweber T, Gatz S, Hannebauer H, Falcon T, Hesse R, Schmidt J, Brendel R. Towards 20% efficient large-area screen-printed rear-passivated silicon solar cells. *Progress in Photovoltaics: Research and Applications* 2012; **20**(6): 630–638. DOI:10.1002/pip.1198.
4. Schmidt J, Veith B, Brendel R. Effective surface passivation of crystalline silicon using ultrathin Al_2O_3 films and $\text{Al}_2\text{O}_3/\text{SiN}_x$ stacks. *Physica Status Solidi (RRL) - Rapid Research Letters* 2009; **3**(9): 287–289. DOI:10.1002/pssr.200903272.
5. Mack S, Jager U, Kastner G, Wotke EA, Belledin U, Wolf A, Preu R, Biro D. Towards 19% efficient industrial PERC devices using simultaneous front emitter and rear surface passivation by thermal oxidation. 35th IEEE PVSC, Honolulu, HI 2010, pp. 34–38. DOI: 10.1109/PVSC.2010.5614048.
6. Schmidt J, Kerr M, Cuevas A. Surface passivation of silicon solar cells using plasma-enhanced chemical-vapour-deposited SiN films and thin thermal SiO_2 /plasma SiN stacks. *Semiconductor Science and Technology* 2001; **16**(3): 164–170. DOI:10.1088/0268-1242/16/3/308.
7. Schmidt J, Lim B, Walter D, Bothe K, Gatz S, Dullweber T, Altermatt PP. Impurity-related limitations of next-generation industrial silicon solar cells. *Photovoltaics, IEEE Journal of* 2013; **3**(1): 114–118. DOI:10.1109/JPHOTOV.2012.2210030.
8. Fischer H, Pschunder W. Investigation of photon and thermal induced changes in silicon solar cells. *Proceedings 10th IEEE PVSC, Palo Alto, CA (IEEE, New York, 1973)* 1974, p. 404.
9. Bothe K, Sinton R, Schmidt J. Fundamental boron-oxygen-related carrier lifetime limit in mono- and multicrystalline silicon. *Progress in Photovoltaics: Research and Applications* 2005; **13**(4): 287–296. DOI:10.1002/pip.586.
10. Schmidt J, Aberle AG, Hezel R. Investigation of carrier lifetime instabilities in Cz-grown silicon. *Proceedings 26th IEEE PVSC, Anaheim, CA (IEEE, New York, 1997)* 1997, p. 13.
11. Schmidt J, Bothe K. Structure and transformation of the metastable boron- and oxygen-related defect center in crystalline silicon. *Physical Review B* 2004; **69**(2): 24107. DOI:10.1103/PhysRevB.69.024107.
12. Herguth A, Schubert G, Kaes M, Hahn G. A new approach to prevent the negative impact of the metastable defect in boron doped Cz silicon solar cells. *Proc. of the 32nd IEEE PVSC (4th WCPEC)*, Waikoloa, USA 2006, pp. 940–943.
13. Walter DC, Lim B, Bothe K, Voronkov VV, Falster R, Schmidt J. Effect of rapid thermal annealing on recombination centres in boron-doped Czochralski-grown silicon. *Applied Physics Letters* 2014; **104**(4): 42111. DOI:10.1063/1.4863674.
14. Glunz SW, Rein S, Warta W, Knobloch J, Wettling W. On the degradation of Cz-silicon solar cells. *Proc. 2nd WC-PVSEC, Vienna, Austria (WIP, Munich, 1998)* 1998, p. 1343.
15. Hallam BJ, Wenham SR, Hamer PG, Abbott MD, Sugianto A, Chan CE, Wenham AM, Eadie MG, Xu GQ. Hydrogen passivation of B-O defects in Czochralski silicon. *Energy Procedia* 2013; **38**: 561–570. DOI:10.1016/j.egypro.2013.07.317.
16. Wilking S, Beckh C, Ebert S, Herguth A, Hahn G. Influence of bound hydrogen states on BO-regeneration kinetics and consequences for high-speed regeneration processes. *Solar Energy Materials and Solar Cells* 2014; **131**: 2–8. DOI:10.1016/j.solmat.2014.06.027.

17. Voronkov VV, Falster R. Light-induced boron-oxygen recombination centres in silicon: understanding their formation and elimination. *Solid State Phenomena (SSP)* 2013; **205–206**: 3–14. DOI:10.4028/www.scientific.net/SSP.205-206.3.
18. Walter DC, Lim B, Bothe K, Falster R, Voronkov VV, Schmidt J. Lifetimes exceeding 1 ms in 1- Ω cm boron-doped Cz-silicon. *Solar Energy Materials and Solar Cells* 2014; **131**: 51–57. DOI:10.1016/j.solmat.2014.06.011.
19. Murphy JD, Bothe K, Krain R, Voronkov VV, Falster RJ. Parameterisation of injection-dependent lifetime measurements in semiconductors in terms of Shockley–Read–Hall statistics: an application to oxide precipitates in silicon. *Journal of Applied Physics* 2012; **111**(11): 113709. DOI:10.1063/1.4725475.
20. Sinton RA, Cuevas A. Contactless determination of current–voltage characteristics and minority-carrier lifetimes in semiconductors from quasi-steady-state photoconductance data. *Applied Physics Letters* 1996; **69**(17): 2510. DOI:10.1063/1.117723.
21. Richter A, Werner F, Cuevas A, Schmidt J, Glunz SW. Improved parameterization of Auger recombination in silicon. *Energy Procedia* 2012; **27**(0): 88–94. DOI:10.1016/j.egypro.2012.07.034.
22. Shockley W, Read WT. Statistics of the Recombinations of Holes and Electrons. *Physical Review* 1952; **87**(5): 835–842. DOI:10.1103/PhysRev.87.835.
23. Bothe K. Oxygen-related trapping and recombination centres in boron-doped crystalline silicon. PhD thesis, University of Hanover 2006.
24. Richter A, Glunz SW, Werner F, Schmidt J, Cuevas A. Improved quantitative description of Auger recombination in crystalline silicon. *Physical Review B* 2012; **86**(16): 165202. DOI:10.1103/PhysRevB.86.165202.
25. Wilking S, Ebert S, Herguth A, Hahn G. Influence of hydrogen effusion from hydrogenated silicon nitride layers on the regeneration of boron-oxygen related defects in crystalline silicon. *Journal of Applied Physics* 2013; **114**(19): 194512. DOI:10.1063/1.4833243.
26. Herguth A, Hahn G. Kinetics of the boron-oxygen related defect in theory and experiment. *Journal of Applied Physics* 2010; **108**: 114509.
27. Herguth A, Schubert G, Kaes M, Hahn G. Further investigations on the avoidance of boron-oxygen related degradation by means of regeneration. Proc. of the 22nd EUPVSEC, Milan, Italy 2007, pp. 893–896.
28. Fell A. A free and fast three-dimensional/two-dimensional solar cell simulator featuring conductive boundary and quasi-neutrality approximations. *IEEE Transactions on Electron Devices* 2013; **60**(2): 733–738. DOI:10.1109/TED.2012.2231415.
29. Brendel R. Modeling solar cells with the dopant-diffused layers treated as conductive boundaries. *Progress in Photovoltaics: Research and Applications* 2012; **20**(1): 31–43. DOI:10.1002/pip.954.
30. Hannebauer H, Dullweber T, Baumann U, Falcon T, Brendel R. 21.2%-efficient fineline-printed PERC solar cell with 5 busbar front grid. *Physica Status Solidi (RRL) - Rapid Research Letters* 2014; **8**(8): 675–679. DOI:10.1002/pssr.201409190.
31. Lim B, Brendemühl T, Berger M, Christ A, Dullweber T. n-PERT back junction solar cells: an option for the next industrial technology generation? Proc. 29th EUPVSEC Amsterdam 2014, pp. 661–665. DOI: 10.4229/EUPVSEC20142014-2DO.4.6
32. Brendel R, Dreissigacker S, Harder N-P, Altermatt PP. Theory of analyzing free energy losses in solar cells. *Applied Physics Letters* 2008; **93**(17): 173503. DOI:10.1063/1.3006053.